3-D Quantification of the Aortic Arch Morphology in 3-D CTA Data for Endovascular Aortic Repair

Stefan Wörz*, Hendrik von Tengg-Kobligk, Verena Henninger, Fabian Rengier, Hardy Schumacher, Dittmar Böckler, Hans-Ulrich Kauczor, and Karl Rohr

***Abstract*—We introduce a new model-based approach for the segmentation and quantification of the aortic arch morphology in 3-D computed tomography angiography (CTA) data for thoracic endovascular aortic repair (TEVAR). The approach is based on a model-fitting scheme using a 3-D analytic intensity model for thick vessels in conjunction with a two-step refinement procedure, and allows us to accurately quantify the morphology of the aortic arch. Based on the fitting results, we additionally compute the (local) 3-D vessel curvature and torsion as well as the relevant lengths not only along the 3-D centerline, but particularly also along the inner and outer contour. These measurements are important for preoperative planning in TEVAR applications. We have validated our approach based on 3-D synthetic as well as 3-D MR phantom images. Moreover, we have successfully applied our approach using 3-D CTA datasets of the human thorax and have compared the results with ground truth obtained by a radiologist. We have also performed a quantitative comparison with a commercial vascular analysis software.**

***Index Terms*—3-D analytic intensity model, 3-D aortic arch segmentation, 3-D computed tomography angiography (CTA) data, endovascular graft (EVG).**

I. Introduction

AORTIC arch repair (AAR) poses a major challenge for surgeons and radiologists due to its tortuous anatomy and relevant side branches (see Fig. 1). Since patients often have significant comorbidities, an increasing number of aortic arch pathologies are treated by semiinvasive procedures using endovascular grafts (EVG, see Fig. 2) [1]. Endovascular aortic repair (EVAR) was initially used for the *abdominal* aorta, but has in recent years also been explored for the *thoracic* aorta comprising the aortic arch. Thoracic EVAR (TEVAR) constitutes a viable alternative to open repair, while minimizing morbidity and 30-day mortality in patients [2]. However, although endovascular interventions are minimally invasive, they are

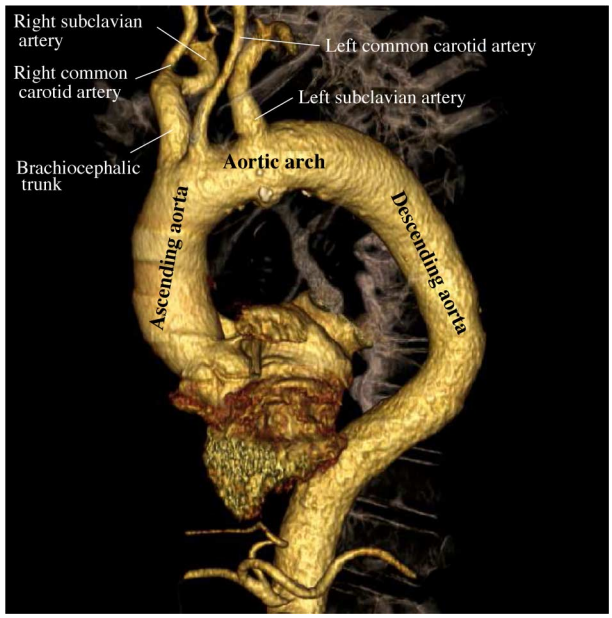

Fig. 1. Anatomy of the thoracic aorta (volume rendering of a CTA dataset).

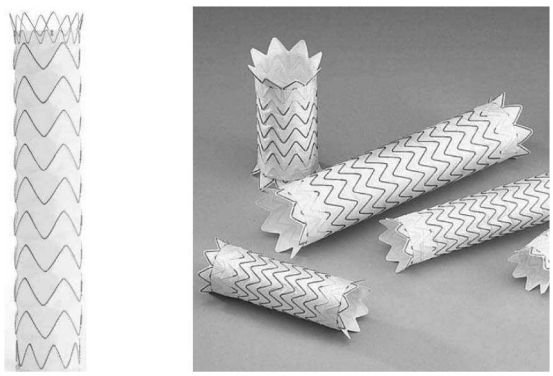

Fig. 2. EVGs from Medtronic (Valiant, left) and W. L. Gore and Associates (TAG, right).

Manuscript received July 31, 2009; revised January 15, 2010 and April 30, 2010; accepted June 12, 2010. Date of publication June 21, 2010; date of current version September 15, 2010. This work was supported by Deutsche Forschungsgemeinschaft (DFG) under Project QuantVessel RO 2471/6, and in part by the Research training group 1126: Intelligent Surgery. *Asterisk indicates corresponding author.*

*S. Wörz is with the Department of Bioinformatics and Functional Genomics, Biomedical Computer Vision Group, University of Heidelberg, BIOQUANT, IPMB, and DKFZ Heidelberg, 69120 Heidelberg, Germany (e-mail: s.woerz@dkfz.de).

H. von Tengg-Kobligk and H.-U. Kauczor are with the Department of Diagnostic and Interventional Radiology, University of Heidelberg, 69120 Heidelberg, Germany (e-mail: h.vontengg@dkfz-heidelberg.de; hans-ulrich.kauczor@med.uni-heidelberg.de).

V. Henninger and F. Rengier are with the Department of Radiology, German Cancer Research Center (DKFZ) Heidelberg, 69120 Heidelberg, Germany (e-mail: v.henninger@dkfz-heidelberg.de; f.rengier@dkfz-heidelberg.de).

H. Schumacher is with the Clinic for Vascular and Endovascular Surgery, Academic Teaching Hospital Hanau, 63450 Hanau, Germany (e-mail: hardy_schumacher@klinikum-hanau.de).

D. Böckler is with the Department of Vascular and Endovascular Surgery, University of Heidelberg, 69120 Heidelberg, Germany (e-mail: dittmar.boeckler@med.uni-heidelberg.de).

K. Rohr is with the Department of Bioinformatics and Functional Genomics, Biomedical Computer Vision Group, University of Heidelberg, BIOQUANT, IPMB, and DKFZ Heidelberg, 69120 Heidelberg, Germany (e-mail: k.rohr@dkfz-heidelberg.de).

Color versions of one or more of the figures in this paper are available online at http://ieeexplore.ieee.org.

Digital Object Identifier 10.1109/TBME.2010.2053539

0018-9294/$26.00 © 2010 IEEE

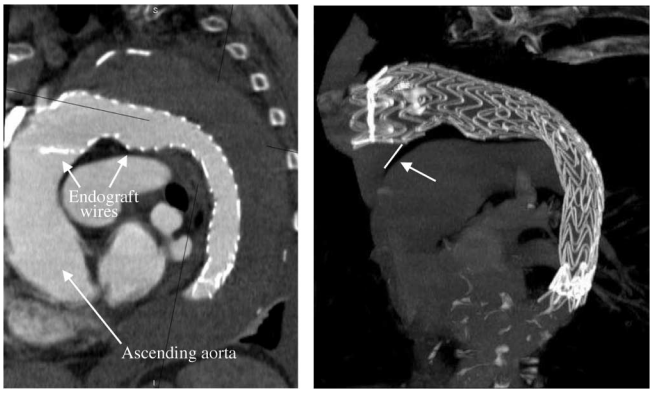

Fig. 3. 2-D section (left) and maximum intensity projection (right) of a 3-D CTA dataset of a patient with clinic type B dissection after implantation of an EVG into the aortic arch beginning distal to the left common carotid artery. The EVG shows a significant misalignment with respect to the inner contour of the proximal aortic arch (see the arrow on the right).

associated with specific complications. The EVGs currently used for AAR were generally designed for the descending aorta, and therefore, fail to represent the curved and tortuous anatomy of the aortic arch, so misalignment of the EVG is often the case [3] (see Fig. 3). This causes endoleaks, reinterventions, and potentially open surgery after initial EVG placement. The optimal EVG for endovascular arch reconstruction is yet to be found. Key requirements of an EVG are flexibility and conformability to comply with the curvature of the aortic arch [3].

In TEVAR, preoperative imaging is crucial to assess the vascular anatomy using, for example, 3-D computed tomography angiography (CTA) (e.g., [4]). For patient and device selection in TEVAR, morphological parameters need to be known, such as aortic diameters, length of pathology along the centerline, and tortuosity of the aorta. In addition, we propose to choose an EVG also based on the relevant lengths along the *outer* and *inner* contours of the aortic arch, which are important, for example, for planning the landing zone of the EVG. In particular, in case the landing zone is *between* two supra aortic branches (the upper three main branches in Fig. 1), accurately measuring the length between the branches along the *outer* contour is crucial. However, whereas in clinical practice, the vessel diameters and lengths along the vessel *centerline* can be measured using commercial tools (e.g., [5]), the lengths along the *inner* and *outer* contour of the curved aortic arch as well as the (local) curvature and torsion of the arch are often not quantified at all, or only manually determined, which is subjective, time consuming, and error prone. Note that for the curved arch the lengths along the contour, in general, significantly deviate from the corresponding length along the centerline (see Section II-C in the following).

Previous work on automatic segmentation of vessels from 3-D images can be divided into two main classes of approaches, one based on differential measures (e.g., [6]–[12]) and the other based on deformable models (e.g., [13]–[25]). For comprehensive surveys on the topic we refer to, for example, [26] and [27]. Approaches based on *differential measures* typically use partial derivatives of the image data up to second order. For example, in [10], the image gradient is exploited, i.e., first-order partial derivatives of an image have to be determined. In contrast, in [6]–[9], [11], and [12], the Hessian matrix is used, which requires second-order partial derivatives of an image (note that in [9] and [11] both the gradient and the Hessian are used). In the latter approaches, eigenvalues and eigenvectors of the Hessian are exploited, and often a vesselness measure is defined based on the eigenvalues (e.g., [7]). While being computationally efficient, a disadvantage of differential measures is their sensitivity to noise, since only local image information is taken into account. The robustness can be improved, for example, by using a multiscale approach (e.g., [6], [7], [9]). On the other hand, approaches based on *deformable models* generally exploit *contour information* of anatomical structures. While these approaches include more global information in comparison to differential approaches, often only 2-D or 3-D contours are taken into account (e.g., [13]–[17]). Alternatively, deformable models using parametric *intensity* models have been suggested (e.g., [28]–[30]). In comparison to contour-based models, more image information is taken into account to improve the robustness and accuracy of the segmentation result.

Concerning the segmentation of the aorta, model-based approaches have been proposed for *abdominal* aortic aneurysms (AAA, e.g., [15], [18]–[20], [22]), i.e., the lower part of the aorta, which is more or less straight, for example, to quantify the lumen and thrombus. Yim *et al.* [15] use a deformable cylindrical surface mesh model to segment the abdominal aorta in contrast-enhanced 3-D MR angiography (MRA) data. The approach exploits the image gradient to attract the deformable model to vessel contours. de Bruijne *et al.* [18] describe an interactive vessel segmentation scheme using an active shape model for 2-D cross sections in 3-D CTA images. The shape model has been trained using manual segmentations of AAA. To segment the contour of an AAA gradient information and grey levels near the contour are used. Chen and Amini [19] use a triangulated surface model in conjunction with level sets for vessel segmentation in 3-D MRA images. In addition, Hessian-based vessel enhancement is used as a preprocessing step. Olabarriaga *et al.* [20] present an approach based on active appearance models for the segmentation of AAA in 3-D CTA images. Grey-level image information is taken into account by sampling along surface normals of the shape model. Egger *et al.* [22] use region-growing and an active contour model for the segmentation of the abdominal aorta in 3-D CTA images. To attract the contour model to the vessel contour, the approach exploits the gradient of a distance transform, which is initialized using the result of region-growing. However, we are not aware of a model-based approach, which has been used to quantify the morphology of the aortic *arch* for preoperative planning of TEVAR using grafts.

In this contribution, we introduce a new model-based approach for the quantification of the morphology of the aortic arch in 3-D CTA datasets for TEVAR (for a preliminary version of this work, see [31]). Our approach is based on a 3-D analytic intensity model, which is directly fitted to the image intensities within 3-D regions-of-interest (ROIs). Fitting results include the local vessel radius and contrast as well as 3-D positions and 3-D orientations along the centerline. In contrast to previous work, we also compute the (local) 3-D vessel curvature and torsion as

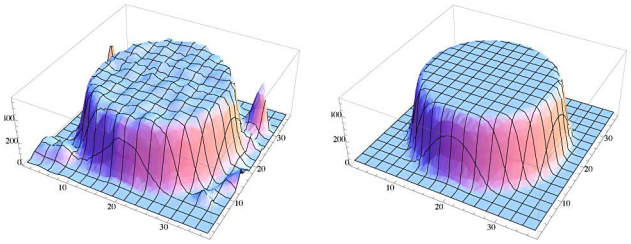

Fig. 4. (Left) 3-D intensity plot of a 2-D section of a 3-D CTA dataset showing the thoracic aorta as well as (right) a 2-D section of a generated 3-D image using the new cylindrical intensity model.

well as the relevant lengths not only along the 3-D centerline, but particularly along the inner and outer contour. This is important for preoperative planning in TEVAR applications. In comparison to previous *contour-based* deformable models (e.g., [15], [18]–[20], [22]) much more image information is taken into account to improve the robustness and accuracy of the segmentation result. In fact, the new model represents both the 3-D shape and the 3-D intensity structure of vessels. Moreover, in contrast to previous approaches based on *intensity* models, our model is particularly suited for vessels of large widths, such as the aorta (e.g., in contrast to [28], [29], where Gaussian models have been used in different applications), and it is computationally more efficient than the model in [30]. In addition, we introduce a two-step refinement procedure to improve the robustness and accuracy of model fitting by using different sizes of the ROI.

This paper is organized as follows. In the following section, we describe our model-based approach. We first present the 3-D intensity model (Section II-A), and then, describe the segmentation and quantification based on model fitting (Section II-B) and the quantification of the aortic arch morphology (Section II-C). We then present experimental results using 3-D synthetic (Section III-A) and 3-D MR phantom images (Section III-B). In Section III-C, experimental results using 3-D CTA datasets are reported, which are compared in Section III-D with ground truth provided by a radiologist, as well as with results using a commercial vascular analysis software. Finally, we give a conclusion in Section IV.

II. Model-Based Quantification of the Aortic Arch

A. 3-D Intensity Model for Thick Vessels

To quantify the morphology of the aortic arch, we have developed a 3-D analytic intensity model. This 3-D model represents the shape as well as the image intensities of the aortic arch within a 3-D ROI. The model consists of an ideal sharp 3-D cylinder convolved with a 3-D Gaussian to incorporate the blurring effect of the image formation process. This cylindrical model comprises parameters for the width of the tubular structure (radius R) and the image blur σ, and is well suited to model tubular structures of different widths, in particular, it allows to represent the plateau-like intensity structure of *thick* vessels, such as the aorta [e.g., see Fig. 4 (left)]. Note that the exact solution of a Gaussian smoothed cylinder cannot be expressed analytically and thus is computationally expensive.

In [30], an approximation of a Gaussian smoothed cylinder has been introduced, which uses two different approximations based on a Gaussian function and a Gaussian error function for thin and thick cylinders, respectively, and which employs blending functions to smoothly switch between both approximations. However, the application here concerns the segmentation of the aorta, which has a large width. Therefore, we here use a different approximation, which is particularly suited for *thick* cylinders. This 3-D approximation is based on a 2-D approximation [32] of a Gaussian smoothed large disk using the Gaussian error function $\Phi(x) = \int_{-\infty}^{x} (2\pi)^{-1/2}\ e^{-\xi^2/2}\, d\xi$, and is defined as follows:

$$g_{\mathrm{Cylinder}'}(\mathbf{x}, R, \sigma) = \Phi\left(\frac{c_2 - 1}{c_1} + c_1\right) \tag{1}$$

where

$$c_1 = \frac{2}{3}\,\sigma\,\frac{\sqrt{\sigma^2 + r^2}}{2\sigma^2 + r^2} \ \text{ and } \ c_2 = \left(\frac{R^2}{2\sigma^2 + r^2}\right)^{1/3} \tag{2}$$

using $\mathbf{x} = (x, y, z)^T$ and $r = \sqrt{x^2 + y^2}$. In comparison to the approximation in [30], the computation of (1) is about two times faster. The main reason is that the Gaussian error function, which computationally is the most expensive operation, needs to be evaluated only once for each voxel in (1), whereas for the approximation in [30], the Gaussian error function has to be computed twice.

Based on (1), the complete 3-D intensity model is constructed by incorporating intensity levels a_0 (surrounding tissue) and a_1 (vessel) as well as a 3-D rigid transform $\mathcal{R}$ with rotation parameters $\boldsymbol{\alpha} = (\alpha, \beta, \gamma)^T$ and translation parameters $\mathbf{x}_0 = (x_0, y_0, z_0)^T$. This results in the 3-D parametric intensity model with a total of ten parameters $\mathbf{p} = (R, a_0, a_1, \sigma, \alpha, \beta, \gamma, x_0, y_0, z_0)^T$

$$g_{M,\mathrm{Cylinder}}(\mathbf{x}, \mathbf{p}) = a_0 + (a_1 - a_0)\ g_{\mathrm{Cylinder}'}(\mathcal{R}(\mathbf{x}, \boldsymbol{\alpha}, \mathbf{x}_0), R, \sigma). \tag{3}$$

For example, Fig. 4 shows a 3-D intensity plot of a 2-D section of a 3-D CTA dataset of the thoracic aorta (left) as well as a 2-D section of a generated 3-D image using the new cylindrical intensity model (right). It can be seen that the new model very well represents the plateau-like intensity structure of the aorta in the original data.

B. Segmentation and Quantification of the Aortic Arch

To segment the aortic arch, we utilize an incremental (segmentwise) process, which starts from a given point D at the descending aorta and proceeds along the aorta until it reaches a given point A at the ascending aorta (see Fig. 5). In each increment, the parameters of a cylinder segment are determined by fitting the cylindrical model $g_{M,\mathrm{Cylinder}}$ to the image intensities $g(\mathbf{x})$ within a 3-D ROI, thus minimizing

$$\sum_{\mathbf{x} \in \mathrm{ROI}} \left(g_{M,\mathrm{Cylinder}}(\mathbf{x}, \mathbf{p}) - g(\mathbf{x})\right)^2. \tag{4}$$

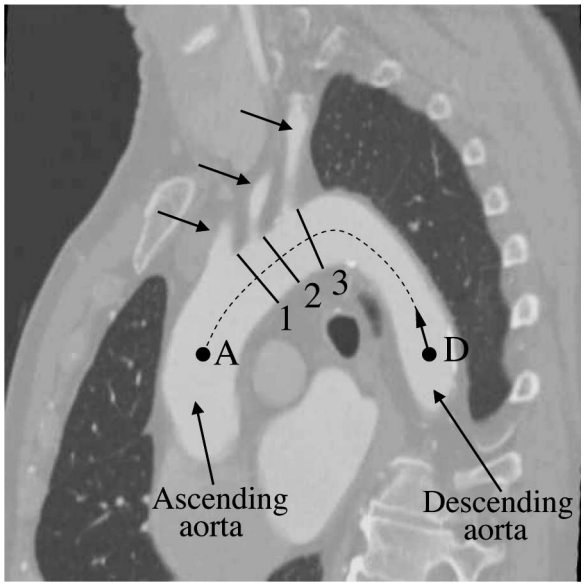

Fig. 5. 2-D section of a 3-D CTA dataset showing the aortic arch with sketched centerline, marked points A and D, and points 1, 2, and 3 distal to the supra aortic branches.

Fig. 6. 3-D segmentation result of the aortic arch overlayed with two orthogonal 2-D sections of the original 3-D CTA dataset.

For minimization, we apply the method of Levenberg–Marquardt (e.g., [33]), incorporating first-order partial derivatives of the cylindrical model with respect to the model parameters. The partial derivatives have been derived analytically. Initial parameters for the fitting process are determined from the estimated parameters of the previous segment using a Kalman filter (e.g., [34]), i.e., the incremental scheme adjusts for varying thickness and changing direction. Note that in our case both the 3-D vessel shape and the 3-D centerline including its 3-D orientation are determined *simultaneously* by model fitting. In contrast, in previous approaches often a subsequent skeletonization step is required to compute the centerline, and the orientation of the centerline is often determined approximately based on the computed skeleton, or not computed at all.

To increase the robustness and accuracy of model fitting, we here apply a *two-step refinement procedure*. In the first step, the aorta is segmented as described earlier using a relatively large size of the 3-D ROI, i.e., more image information is included to robustly estimate the position $\mathbf{x}_0$ and orientation parameters $\boldsymbol{\alpha}$ defining the centerline. The size and shape of the 3-D ROI are automatically adapted to the local shape of the aorta based on the fitting results (i.e., the estimated radius and orientation). In the second step, the estimates for the remaining parameters, such as the radius are *refined* by applying the model to the same cylinder segment again (using the estimated parameters from the first step as initial parameters), but using a smaller size of the ROI in the direction of the centerline to increase the accuracy. Note that both steps use the original image data, i.e., in comparison to multiscale approaches different image scales and image smoothing are not required.

Prior to model fitting, we perform two preprocessing steps. First, to achieve isotropic image data an interpolation based on cubic polynomials [35] is applied. Second, the image intensities are clipped. The reason is that with our model we assume one intensity level a_0 for the surrounding tissue within the 3-D ROI. However, the aortic arch is located close to the air-filled lung (see Fig. 5), which has quite different intensity values (≈ -800 HU) compared to the surrounding tissue of the aorta (≈ 0 HU). Thus, intensity values below 0 HU are set to 0 HU.

C. Quantification of the Aortic Arch Morphology

By applying our approach described earlier, we obtain estimates for the model parameters $\mathbf{p}$ for each vessel segment. In particular, based on the estimated radius R, position $\mathbf{x}_0$, and orientation $\boldsymbol{\alpha}$, we yield a 3-D description of the shape of the aortic arch. For example, Fig. 6 shows the computed 3-D shape of the aortic arch overlayed with two orthogonal sections of the original 3-D image data.

In addition to the estimated positions $\mathbf{x}_{0,k}$ along the centerline, the centerline can also be characterized by its curvature and torsion; whereas, the curvature measures the bending of the centerline, the torsion describes how sharply it is twisting. To compute the (local) 3-D curvature κ and torsion τ of the centerline of the aortic arch, we apply a least-squares approach using 3-D parametric curves $\mathbf{p}_k(t) = (p_{x,k}(t), p_{y,k}(t), p_{z,k}(t))^T$ defined by the parameter t, which are locally fitted to a range of centerline positions $\mathbf{x}_{k-r}, \ldots, \mathbf{x}_k, \ldots, \mathbf{x}_{k+r}$. In our case, we use cubic polynomials $p_k(t) = c_3 t^3 + c_2 t^2 + c_1 t + c_0$ for the x-, y-, and z-components of the curve, and for the range, we use $r = 7$. By fitting the parametric curve $\mathbf{p}_k(t)$ to the centerline points within a local range, we obtain estimates for the coefficients c_0, c_1, c_2, and c_3 for all three components of the curve. For the kth position of the centerline, the curvature and torsion can then be computed by (e.g., [36], [37])

$$\kappa_k = \frac{|\mathbf{p}'_k \times \mathbf{p}''_k|}{|\mathbf{p}'_k|^3} \quad \text{and} \quad \tau_k = \frac{|\mathbf{p}'_k \, (\mathbf{p}''_k \times \mathbf{p}'''_k)|}{|\mathbf{p}'_k \times \mathbf{p}''_k|^2} \tag{5}$$

where $\mathbf{p}'_k$, $\mathbf{p}''_k$, and $\mathbf{p}'''_k$ denote first-, second-, and third-order derivatives of $\mathbf{p}_k(t)$ with respect to t, respectively. The derivatives can be directly computed from the fitted cubic polynomials,

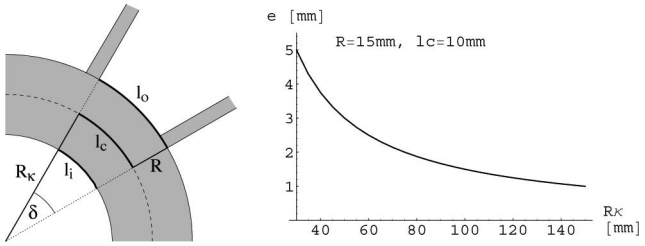

Fig. 7. Sketch of a curved aortic arch (left) showing the radius R, the radius of curvature R_κ, as well as the corresponding lengths l_i, l_c, and l_o along the inner contour, the centerline, and the outer contour, respectively. The diagram (right) shows the absolute difference between the length of the centerline and the inner/outer contour as a function of R_κ for $R = 15$ mm and $l = 10$ mm.

for example, the first-, second-, and third-order derivatives of the x-component are given by $p'_{x,k}(t) = 3\,c_3 t^2 + 2\,c_2 t + c_1$, $p''_{x,k}(t) = 6\,c_3 t + 2\,c_2$, and $p'''_{x,k}(t) = 6\,c_3$. The derivatives for the y- and z-components can be computed analogously. For a given curvature κ, the radius of curvature R_κ is computed by $R_\kappa = \kappa^{-1}$.

To visualize the segmentation results within a 2-D figure and to compute the lengths along the inner and outer contour of the curved aortic arch, we project the segmentation results onto a plane. In our case, this plane is specified by the centerline points A and D as well as the most anterior (highest) point along the centerline. For example, Fig. 10 shows the projected plane and the centerline (dashed), the inner and outer contour (white), as well as the points A, 1, 2, 3, and D, where the points 1, 2, and 3 are distal to the three supra aortic branches. In addition, at several positions along the centerline, the estimated diameters are visualized by lines. Note that for the curved arch, the lengths along the contour, in general, significantly deviate from the corresponding length along the centerline. To illustrate this, Fig. 7 (left) shows a sketch of a curved aortic arch with two branching vessels. For a radius R of the aorta, a radius of curvature R_κ, and a certain length l_c along the centerline, the lengths l_i and l_o along the inner and outer contour, respectively, compute to

$$l_i = l_c - l_c \frac{R}{R_\kappa} \quad \text{and} \quad l_o = l_c + l_c \frac{R}{R_\kappa} \tag{6}$$

i.e., the absolute difference between the lengths along the contour and the centerline is given by $e(R, R_\kappa, l_c) = l_c - l_i = l_o - l_c = l_c(R/R_\kappa)$. For example, for a typical radius of the thoracic aorta of $R = 15$ mm, a radius of curvature $R_\kappa = 55$ mm, and a length $l_c = 10$ mm, the lengths along the inner and outer contour are $l_i \approx 7.3$ mm and $l_o \approx 12.7$ mm, respectively, i.e., the difference is about $e \approx 2.7$ mm. Fig. 7 (right) shows the difference e as a function of the radius of curvature R_κ for $R = 15$ mm and $l_c = 10$ mm. It can be seen that for small curvatures (large values of R_κ), the difference is about $e \approx 1$ mm (10%), while for larger curvatures, the difference can reach $e \approx 5$ mm (50%) for realistic values of the parameters.

III. Experimental Results

In this section, we present experimental results of applying our 3-D segmentation and quantification approach. First, segmentation results are shown for 3-D synthetic images of curved tubular structures and for a 3-D MR image of a tubular phantom. Moreover, we have applied the new approach to segment ten 3D CTA datasets of the human thorax comprising the aortic arch. The results are compared with ground truth provided by a radiologist as well as with a commercial vascular analysis software

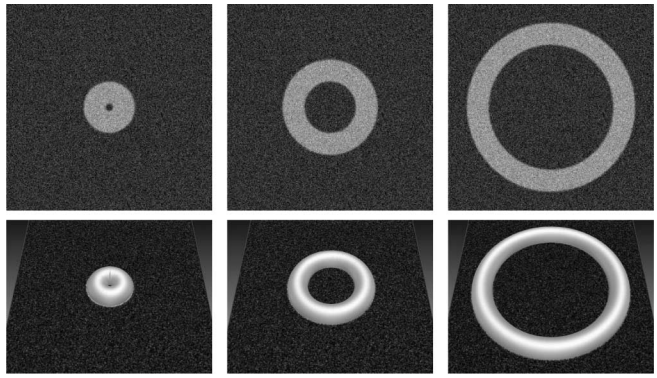

Fig. 8. 2-D cross sections (top) and 3-D segmentation results (bottom) of 3-D synthetic tori of different radii of curvature $R_\kappa = 20$ vox (left), $R_\kappa = 50$ vox (middle), and $R_\kappa = 100$ vox (right) using $R = 15$ vox, $\sigma = 1$ vox, as well as a contrast of $a = 100$ and additional Gaussian noise ($\sigma_n = 20$).

A. 3-D Synthetic Images

To analyze the performance of the new approach, we have generated different 3-D synthetic images containing curved tubular structures using Gaussian smoothed tori with different parameter settings. The images comprise also different levels of additive Gaussian noise. For example, we have generated 3-D images of smoothed tori using nine different radii of curvature $R_\kappa = 20, 30, \ldots, 100$ vox (distance from the centerpoint of the torus to the centerline position of the ring), thus representing curvatures of $\kappa = 0.05, \ldots, 0.01$ vox^{-1}, as well as using a radius of $R = 15$ vox and Gaussian smoothing with standard deviation $\sigma = 1$ vox (*vox* denotes the spatial unit in 3-D, i.e., one voxel is a cube with a size of one *vox* in each dimension). The image contrast was set to $a = 100$ and the standard deviation of the added Gaussian noise to $\sigma_n = 20$. Fig. 8 (top) shows 2-D cross sections for $R_\kappa = 20$ vox (left), $R_\kappa = 50$ vox (middle), and $R_\kappa = 100$ vox (right). Note that very large curvatures, such as $R_\kappa = 20$ vox are anatomically not realistic for the thoracic aorta, however, we have included them to explore the limits of the proposed approach.

In all 3-D images of the tori, the segmentation and quantification was successful. For example, Fig. 8 (bottom) shows the computed 3-D shapes for three tori overlayed with one section of the original 3-D image data (top). Moreover, the results for the estimated radius R, radius of curvature R_κ, and curvature κ for nine tori with varying curvature are summarized in Table I. We have computed the mean error $\bar{e}$ and the maximal error $e_{\max}$ over all segments of the tori as determined by the incremental segmentation scheme (between 183 and 695 segments in this experiment). It turns out that the radius R was quite well

TABLE I
SUMMARY OF 3-D SEGMENTATION RESULTS FOR NINE TORI WITH VARYING CURVATURE: MEAN ERROR $\bar{e}$ AND MAXIMAL ERROR $e_{\max}$ OF THE ESTIMATED RADIUS (IN VOX), RADIUS OF CURVATURE (IN VOX), AND CURVATURE (IN VOX^{-1}), COMPUTED OVER ALL SEGMENTS OF THE TORI

		Radius		Radius of curv.		Curvature	
R_κ	κ	$\bar{e}_R$	$e_{max,R}$	$\bar{e}_{R_\kappa}$	e_{max,R_κ}	$\bar{e}_\kappa$	$e_{max,\kappa}$
20	0.05000	0.35	0.41	1.23	1.50	0.00329	0.00406
30	0.03333	0.14	0.18	0.71	1.30	0.00082	0.00152
40	0.02500	0.07	0.11	0.51	1.21	0.00032	0.00078
50	0.02000	0.04	0.07	0.52	1.65	0.00021	0.00068
60	0.01667	0.02	0.05	0.54	1.36	0.00015	0.00039
70	0.01429	0.01	0.05	0.61	2.08	0.00012	0.00044
80	0.01250	0.01	0.04	0.60	2.22	0.00009	0.00036
90	0.01111	0.01	0.05	0.86	3.10	0.00011	0.00037
100	0.01000	0.01	0.04	0.91	3.81	0.00009	0.00040

estimated with a maximal error of $e_{\max,R} = 0.41$ vox over all nine tori, which is well in the subvoxel range. Excluding the tori with the highest curvature, the error is much smaller with $e_{\max,R} \leq 0.07$ vox for $R_\kappa \geq 50$ vox. For the radius of curvature R_κ, the mean error $\bar{e}_{R_\kappa}$ and the maximal error $e_{\max,R_\kappa}$ are well below 2.5% and 5% compared to the correct value, respectively, except for the case of the very high curvature $R_\kappa = 20$ vox (cf., Fig. 8, left). However, even in this case, the obtained maximal error is only $e_{\max,R_\kappa} = 1.5$ vox, which is still a relatively good result. Note that the errors $\bar{e}_{R_\kappa}$ and $e_{\max,R_\kappa}$ are slightly increasing for larger radii of curvature $R_\kappa \geq 70$. The reason is that with increasing R_κ, the torus is locally less curved, which naturally makes it more difficult to estimate R_κ with high accuracy (note that the presented errors are *absolute* values). However, the *relative* errors with respect to R_κ are not affected. The results for the mean $\bar{e}_\kappa$ and the maximal error $e_{\max,\kappa}$ of the curvature κ in Table I are analogous to those of the radius of curvature R_κ.

B. 3-D MR Phantom Image

To further validate our approach, we created a 3-D MR image of a tubular phantom. The tubular phantom is made of acrylic glass and has a length of about 160 mm and an inner radius of $R_i = 15.50$ mm. The tubular phantom was filled with a gadolinium-based contrast agent (gadopentetate dimeglumine (Gd-DTPA), Schering, Berlin, Germany) and Iomeprol (400 mg I/ml, Bracco–Altana Pharma, Konstanz, Germany), and was scanned with a standard clinical 1.5 T whole-body system (Avanto, Siemens). The resulting 3-D phantom image has a size of $512 \times 512 \times 80$ voxels with an isotropic resolution of 0.78 mm. Fig. 9 (left) shows a 2-D longitudinal section of the tubular phantom.

The results of applying our approach to segment the 3-D MR phantom image are presented in Table II. The table shows the estimated radius $\hat{R}$ and the error $e_R = |\hat{R} - R_i|$ for ten cross sections. The mean error is $\bar{e}_R = 0.46$ mm, which is about half of the image resolution. Fig. 9 (center) shows the 3-D segmentation result overlayed with two orthogonal 2-D sections of the MR image. Moreover, Fig. 9 (right) shows one 2-D cross section overlayed with the segmentation result, where the contour

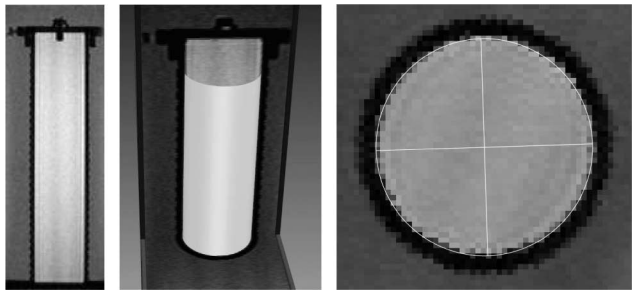

Fig. 9. 3-D MR image of a tubular phantom. (Left) 2-D longitudinal section. (Center) 3-D segmentation result. (Right) 2-D cross section overlayed with segmentation result.

TABLE II
3-D SEGMENTATION RESULTS FOR A 3-D MR IMAGE OF A TUBULAR PHANTOM: ESTIMATED RADIUS $\hat{R}$ AND ERROR e_R OF THE ESTIMATED RADIUS AS WELL AS ERROR $e_{\rm pos}$ OF THE ESTIMATED POSITION OF THE CENTERLINE (ALL IN MM) FOR TEN DIFFERENT SECTIONS OF THE TUBULAR PHANTOM

Section	$\hat{R}$	e_R	e_{pos}
1	15.95	0.45	0.09
2	15.96	0.46	0.08
3	15.96	0.46	0.39
4	15.96	0.46	0.27
5	15.96	0.46	0.39
6	15.97	0.47	0.38
7	15.97	0.47	0.31
8	15.96	0.46	0.25
9	15.96	0.46	0.22
10	15.95	0.45	0.35
Mean	15.96	0.46	0.27

as well as the diameter and position of the centerline (intersection point of the two lines) are highlighted. It can be seen that the tubular phantom has been segmented quite well.

In addition, we investigated the accuracy of the estimated position of the centerline. Ground truth was determined by a radiologist, who interactively determined the position of the centerline for ten cross sections. The error $e_{\rm pos}$ of the estimated position of the centerline is shown in Table II. The mean error is $\bar{e}_{\rm pos} = 0.27$ mm, which is also well below image resolution and is about a factor of two smaller than the mean error for the radius.

C. 3-D CTA Datasets

We also applied our model-based approach to quantify the morphology of the aortic arch in ten 3-D multislice CTA datasets. The patients were scanned with a 16-slice CT scanner (Aquilion 16, Toshiba, Japan) using an iodinated contrast medium (Iomeprol, 400 mg I/ml). The 3-D images comprise 619 to 829 slices with a slice spacing of 0.8 mm. Each slice consists of 512×512 voxels and has a within-slice resolution between 0.512 and 0.625 mm. For each 3-D image, we specified a point D at the descending aorta as a starting point for segmentation as well as a point A at the ascending aorta as end point (see Fig. 5). In all ten 3-D images, the segmentation and quantification of the aortic arch was successful. As an example, Fig. 6 displays the

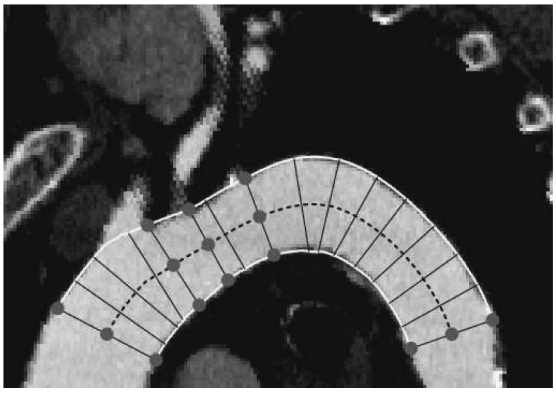

Fig. 10. Projected 2-D plane showing the aortic arch of the first 3-D CTA dataset, where the centerline (dashed), the inner and outer contour (white), the points A, 1, 2, 3, and D, as well as several estimated diameters are marked.

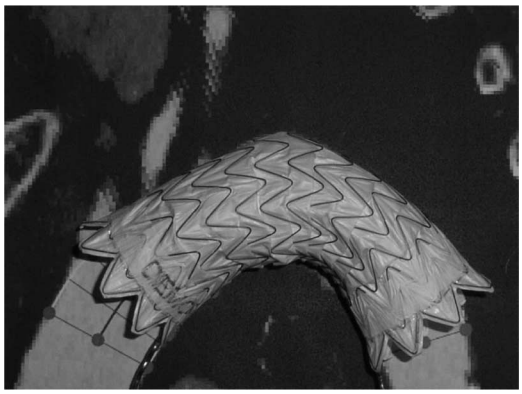

Fig. 11. Picture shows a graft, which has been aligned in accordance with the segmented shape of the aortic arch shown in Fig. 10.

computed 3-D shape for the aortic arch of the first 3-D image. In addition, Fig. 10 shows the 2-D projection of the segmentation result, where the points A, 1, 2, 3, and D at the centerline as well as the inner and outer contour are marked. To illustrate the application of the segmentation results for preoperative planning of TEVAR using a graft, Fig. 11 shows a picture of a graft, which has been aligned in accordance with the segmented shape of the aortic arch (see Fig. 10).

Two-dimensional projections of the segmentation result for the second up to tenth 3-D image are displayed in Fig. 12 (from top-left to bottom-right). Moreover, Table III lists for the first 3-D image the estimated radius of the aorta, radius of curvature, and torsion at the points A, 1, 2, 3, and D, as well as lengths between these points along the inner and outer contour and along the centerline. It can be seen that the lengths along the inner and outer contour significantly differ from the corresponding lengths along the centerline.

The computation time for segmenting the aortic arch is about 40 s for the first step and 20 s for the second step (on a PC with Intel Core2 Quad CPU (2.4 GHz) running Linux).

TABLE III
ESTIMATED RADIUS OF THE AORTA, RADIUS OF CURVATURE, AND TORSION AT THE POINTS A, 1, 2, 3, AND D AS WELL AS LENGTHS BETWEEN THESE POINTS ALONG THE INNER AND OUTER CONTOUR AS WELL AS ALONG THE CENTERLINE FOR THE FIRST 3-D CTA DATASET

[*mm*]	A	1	2	3	D
Radius of aorta	16.68	15.02	14.04	14.17	12.97
Radius of curvature	47.91	123.52	81.95	39.22	52.22
Torsion	-0.013	-0.053	0.005	0.019	0.102
Lengths along	A to 1	1 to 2	2 to 3	3 to D	
inner contour	22.47	11.29	15.49	54.82	
centerline	29.44	12.20	17.54	76.72	
outer contour	38.03	13.30	19.68	98.93	

D. 3-D CTA Datasets: Validation Based on Ground Truth

To validate our approach in the case of the 3-D CTA datasets, we compared the experimental results with ground truth, which was manually obtained by a radiologist performing measurements on multiplanar reformations. In addition, the results were compared with the results obtained using a dedicated workstation with a commercial vascular analysis software as well as with the results of a region-growing approach. For the aortic arch of the first 3-D image (see Fig. 10), the radiologist manually estimated the radius of the aortic arch in steps of 2 mm along the centerline yielding 70 measurements. Fig. 13 shows the estimated radius of the aortic arch for the new approach (bold) and the segmentation results of the radiologist (small grey squares and grey line) as well as for the commercial software (dashed). It turns out that our approach yields a much better result with respect to the ground truth than the commercial software. The maximal difference of the estimated radius between our approach and that of the radiologist is $e_{\max,R} = 1.02$ mm for all 70 measured radii, the mean error is $\bar{e}_R = 0.34$ mm, which is well below image resolution, and the standard deviation is $\sigma_R = 0.26$ mm. In contrast, the commercial software yields a maximal error of $e_{\max,R} = 3.26$ mm, a mean error of $\bar{e}_R = 0.44$ mm, and a standard deviation of $\sigma_R = 0.53$ mm. In particular, the commercial software has problems at the three supra aortic branches, where the radius has been overestimated (dashed), see the left side of the vertical lines 1, 2, and 3 (see Fig. 13). In contrast, using our approach, the estimated radius is hardly affected by the supra aortic branches, and thus, yields more accurate segmentation results. Furthermore, the region-growing approach yields a maximal error of $e_{\max,R} = 2.83$ mm, a mean error of $\bar{e}_R = 1.23$ mm, and a standard deviation of $\sigma_R = 0.46$ mm. The larger maximal error is explained by the fact that region-growing leaks into the supra aortic branches. By manually correcting the results at the branches, the results improve ($e_{\max,R} = 1.96$ mm, $\bar{e}_R = 1.17$ mm, and $\sigma_R = 0.42$ mm), however, the results are still significantly worse compared to our approach.

Moreover, for all ten 3-D datasets, we have compared the estimated radius of the aorta using our approach with the radius determined by the radiologist at the 3-D points A, 1, 2, 3, and D. It turned out that the results of our approach well agree with the ground truth with a maximal error over all points in all 3-D images of $e_{\max,R} = 1.31$ mm, a mean error of $\bar{e}_R = 0.38$ mm, and a standard deviation of $\sigma_R = 0.31$ mm.

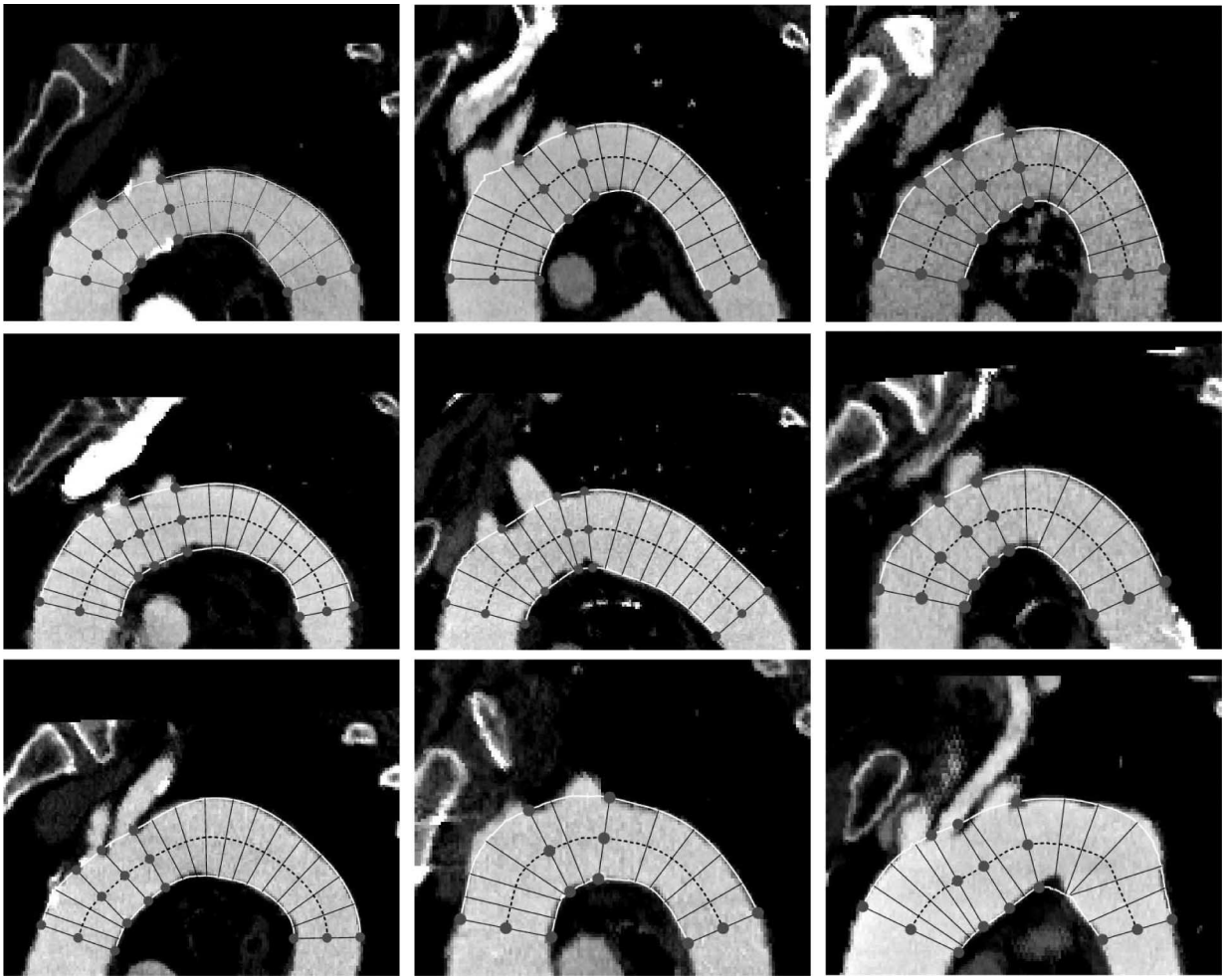

Fig. 12. Same as Fig. 10 for the second to tenth 3-D CTA datasets (from top-left to bottom-right).

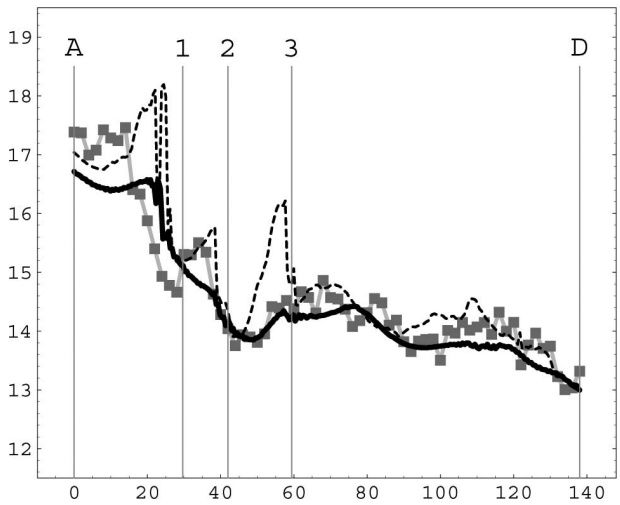

Fig. 13. Diagram shows the estimated radius (in millimeters) of the aortic arch for the new approach (bold), the segmentation results of a radiologist (grey), and the result of the commercial software (dashed).

IV. Conclusion

We introduced a new model-based approach for the segmentation and quantification of the morphology of the aortic arch in 3-D CTA datasets for TEVAR. The approach is based on a 3-D analytic intensity model, which is particularly suited for vessels of large widths. This model is directly fitted to the image intensities to estimate the model parameters. To increase the robustness and accuracy of model fitting, we suggested a two-step refinement procedure, which uses a larger size of the 3-D ROI in the first step to estimate the position and orientation of the centerline and which uses a smaller ROI size in the second step to accurately estimate the radius. Based on the fitting results, we directly compute the (local) 3-D vessel curvature and torsion as well as the relevant lengths along the 3-D centerline and along the inner and outer contour, which are important parameters to assess if and how TEVAR can be applied.

We have validated our approach based on 3-D synthetic images of curved tubular structures as well as using a 3-D MR image of a tubular phantom. The experiments demonstrated that the approach allows to quantify the radius and curvature as well as the position of the centerline highly accurately. In particular, the errors of the estimated radius and position of the centerline are well below image resolution. Moreover, we have successfully applied our approach using ten 3-D CTA datasets and have compared the results with ground truth obtained by a radiologist. It turned out that the new approach accurately estimates the

radius of the aortic arch. Finally, we quantitatively compared our approach with a commercial vascular analysis software as well as with a region-growing approach. The comparison showed that our approach yields superior segmentation results.

Using the proposed model-based approach, it is possible to quantify relevant morphological parameters of the aortic arch, which are important for preoperative planning in TEVAR applications. Future work involves the use of these parameters to preoperatively choose a suitable EVG for an individual patient, for example, based on geometric simulations.

ACKNOWLEDGMENT

The authors would like to thank H. Heckmann, A. Biesdorf, H. Failmezger, and T. Heinemann for implementing the user interface of the segmentation program.

REFERENCES

[1] H. Schumacher, D. Böckler, H. von Tengg-Kobligk, and J.-R. Allenberg, "Acute traumatic aortic tear: Open versus stent-graft repair," *Semin. Vasc. Surg.*, vol. 19, no. 1, pp. 48–59, 2006.

[2] H. Rousseau, J. Bolduc, C. Dambrin, G. Marcheix, B. Canevet, and P. Otal, "Stent-graft repair of thoracic aortic aneurysms," *Tech. Vasc. Intervent. Radiol.*, vol. 8, no. 1, pp. 61–72, 2005.

[3] H. Schumacher, D. Böckler, S. Ockert, and H. von Tengg-Kobligk, "Endovaskuläre Hybridoperationen im Aortenbogen—quo vadis?" *Gefässchirurgie*, vol. 14, pp. 219–229, 2009.

[4] R. Greenberg, J. Secor, and T. Painter, "Computed tomography assessment of thoracic aortic pathology," *Semin. Vasc. Surg.*, vol. 17, no. 2, pp. 166–172, 2004.

[5] M. Lell, K. Anders, M. Uder, E. Klotz, H. Ditt, F. Vega-Higuera, T. Boskamp, W. Bautz, and B. Tomandl, "New techniques in CT angiography," *RadioGraphics*, vol. 26, pp. 45–62, 2006.

[6] T. Koller, G. Gerig, G. Székely, and D. Dettwiler, "Multiscale Detection of Curvilinear Structures in 2-D and 3-D Image Data," in *Proc. 5th Int. Conf. Comput. Vis.* Cambridge, MA: IEEE Computer Society Press, Jun. 1995, pp. 864–869.

[7] A. Frangi, W. Niessen, K. Vincken, and M. Viergever, "Multiscale vessel enhancement filtering," in *Proc. 1st Int. Conf. Med. Image Comput. Comput.-Assist. Intervent.*, ser. Lecture Notes in Computer Science, W. Wells, A. Colchester, and S. Delp, Eds., vol. 1496. Cambridge, MA/Berlin Heidelberg, Germany: Springer-Verlag, Oct. 1998, pp. 130–137.

[8] Y. Sato, S. Nakajima, N. Shiraga, H. Atsumi, S. Yoshida, T. Koller, T. Gerig, and R. Kikinis, "Three-dimensional multi-scale line filter for segmentation and visualization of curvilinear structures in medical images," *Med. Image Anal.*, vol. 2, no. 2, pp. 143–168, 1998.

[9] K. Krissian, G. Malandain, N. Ayache, R. Vaillant, and Y. Trousset, "Model-based detection of tubular structures in 3D images," *Comput. Vis. Image Understand.*, vol. 80, no. 2, pp. 130–171, 2000.

[10] O. Wink, W. Niessen, and M. Viergever, "Fast delineation and visualization of vessels in 3D angiographic images," *IEEE Trans. Med. Imag.*, vol. 19, no. 4, pp. 337–346, Apr. 2000.

[11] S. Aylward and E. Bullitt, "Initialization, noise, singularities, and scale in height ridge traversal for tubular object centerline extraction," *IEEE Trans. Med. Imag.*, vol. 21, no. 2, pp. 61–75, Feb. 2002.

[12] R. Manniesing, M. Viergever, and W. Niessen, "Vessel enhancing diffusion: A scale space representation of vessel structure," *Med. Image Anal.*, vol. 10, pp. 815–825, 2006.

[13] D. Rueckert, P. Burger, S. Forbat, R. Mohiaddin, and G. Yang, "Automatic tracking of the aorta in cardiovascular MR images using deformable models," *IEEE Trans. Med. Imag.*, vol. 16, no. 5, pp. 581–590, Oct. 1997.

[14] A. Frangi, W. Niessen, R. Hoogeveen, V. T. Walsum, and M. Viergever, "Model-based quantitation of 3D magnetic resonance angiographic images," *IEEE Trans. Med. Imag.*, vol. 18, no. 10, pp. 946–956, Oct. 1999.

[15] P. Yim, J. Cebral, R. Mullick, H. Marcos, and P. Choyke, "Vessel surface reconstruction with a tubular deformable model," *IEEE Trans. Med. Imag.*, vol. 20, no. 12, pp. 1411–1421, Dec. 2001.

[16] M. Hernández-Hoyos, M. Orkisz, P. Puech, C. Mansard-Desbleds, P. Douek, and I. Magnin, "Computer-assisted analysis of three-dimensional MR angiograms," *RadioGraphics*, vol. 22, no. 2, pp. 421–435, 2002.

[17] T. Behrens, K. Rohr, and H. Stiehl, "Robust segmentation of tubular structures in 3D medical images by parametric object detection and tracking," *IEEE Trans. Syst., Man, Cybern.*, vol. 33, no. 4, pp. 554–561, Aug. 2003.

[18] M. de Bruijne, B. van Ginneken, M. Viergever, and W. Niessen, "Interactive segmentation of abdominal aortic aneurysms in CTA images," *Med. Image Anal.*, vol. 8, pp. 127–138, 2004.

[19] J. Chen and A. Amini, "Quantifying 3-D vascular structures in MRA images using hybrid PDE and geometric deformable models," *IEEE Trans. Med. Imag.*, vol. 23, no. 10, pp. 1251–1262, Oct. 2004.

[20] S. Olabarriaga, J.-M. Rouet, M. Fradkin, M. Breeuwer, and W. Niessen, "Segmentation of thrombus in abdominal aortic aneurysms from CTA with nonparametric statistical grey level appearance modeling," *IEEE Trans. Med. Imag.*, vol. 24, no. 4, pp. 477–485, Apr. 2005.

[21] J. Tyrrell, E. di Tomaso, D. Fuja, R. Tong, K. Kozak, R. Jain, and B. Roysam, "Robust 3-D modeling of vasculature imagery using superellipsoids," *IEEE Trans. Med. Imag.*, vol. 26, no. 2, pp. 223–237, Feb. 2007.

[22] J. Egger, S. Großkopf, and B. Freisleben, "Simulation of bifurcated stent grafts to treat abdominal aortic aneurysms (AAA)," in *Proc. SPIE Medical Imaging 2007: Visualization and Image-Guided Procedures*, ser. Proc. SPIE, K. Cleary and M. Miga, Eds., vol. 6509. San Diego, CA/Bellingham, WA: SPIE, Feb.

[23] A. Gooya, H. Liao, K. Matsumiya, K. Masamune, Y. Masutani, and T. Dohi, "A variational method for geometric regularization of vascular segmentation in medical images," *IEEE Trans. Med. Imag.*, vol. 27, no. 8, pp. 1295–1312, Aug. 2008.

[24] D.-G. Kang, D. Suh, and J. Ra, "Three-dimensional blood vessel quantification via centerline deformation," *IEEE Trans. Med. Imag.*, vol. 28, no. 3, pp. 405–414, Mar. 2009.

[25] Q. Song, X. Wu, X. Dou, and M. Sonka, "Globally optimal 3-D graph search incorporating both edge and regional information: Application to aortic MR image segmentation," in *Proc. SPIE Medical Imaging 2009: Image Processing*, ser. Proc. SPIE, J. Pluim and B. Dawant, Eds. Lake Buena Vista, FL/Bellingham, WA: SPIE, Feb.

[26] C. Kirbas and F. Quek, "A review of vessel extraction techniques and algorithms," *ACM Comput. Surv.*, vol. 36, no. 2, pp. 81–121, 2004.

[27] A. Giachetti and G. Zanetti, "Vascular modeling from volumetric diagnostic data: A review," *Curr. Med. Imag. Rev.*, vol. 2, pp. 415–423, 2006.

[28] H. Noordmans and A. Smeulders, "High accuracy tracking of 2D/3D curved line structures by consecutive cross-section matching," *Pattern Recognit. Lett.*, vol. 19, no. 1, pp. 97–111, 1998.

[29] A. Bhalerao, E. Thönnes, W. Kendall, and R. Wilson, "Inferring vascular structure from 2D and 3D imagery," in *Proc. Fourth Internat. Conf. Med. Image Comput. Computer-Assisted Interven.*, ser. Lecture Notes in Computer Science, W. Niessen and M. Viergever, Eds., vol. 2208. Utrecht, The Netherlands/Berlin, Heidelberg, Germany: Springer-Verlag, Oct. 2001.

[30] S. Wörz and K. Rohr, "Segmentation and quantification of human vessels using a 3-D cylindrical intensity model," *IEEE Trans. Image Process.*, vol. 16, no. 8, pp. 1994–2004, Aug. 2007.

[31] S. Wörz, H. von Tengg-Kobligk, V. Henninger, D. Böckler, H.-U. Kauczor, and K. Rohr, "Quantification of the aortic arch morphology in 3D CTA images for endovascular aortic repair (EVAR)," in *Proc. SPIE Medical Imaging 2008: Visualization, Image-guided Procedures, and Modeling*, ser. Proc. SPIE, M. Miga and K. Cleary, Eds. San Diego, CA/Bellingham, WA: SPIE, Feb.

[32] M. Abramowitz and I. Stegun, *Pocketbook of Mathematical Functions*. Germany: Verlag Harri Deutsch, Thun und Frankfurt/Main, 1984.

[33] W. Press, B. Flannery, S. Teukolsky, and W. Vetterling, *Numerical Recipes in C*. Cambridge, U.K.: Cambridge Univ. Press, 1992.

[34] R. Kalman, "A new approach to linear filtering and prediction problems," *Trans. ASME-J. Basic Eng.*, vol. 82 (Series D), pp. 35–45, 1960.

[35] E. Meijering, K. Zuiderveld, and M. Viergever, "Image reconstruction by convolution with symmetrical piecewise nth-order polynomial kernels," *IEEE Trans. Image Process.*, vol. 8, no. 2, pp. 192–201, Feb. 1999.

[36] G. Grosche, V. Ziegler, D. Ziegler, and E. Zeidler, Eds., *Teubner-Taschenbuch der Mathematik, Teil I*, 1st ed. B. G. Teubner, Stuttgart, Leipzig, 1996.

[37] R. Medina, A. Wahle, M. Olszewski, and M. Sonka, "Curvature and torsion estimation for coronary-artery motion analysis," in *Proc. SPIE Medical Imaging 2004: Physiology, Function, and Structure from Medical Images* ser. Proc. SPIE, A. Amini and A. Manduca, Eds., vol. 5369. San Diego, CA/Bellingham, WA: SPIE, May, pp. 504–515.

Stefan Wörz received the Diploma degree in informatics and the Ph.D. degree in medical image analysis from the University of Hamburg, Hamburg, Germany, in 2000 and 2006, respectively.

From 2001 to 2004, he was in the School of Information Technology, International University in Germany, Bruchsal, Germany. Since 2005, he has been a Research Associate at the University of Heidelberg, IPMB, BIOQUANT, and the German Cancer Research Center (DKFZ) Heidelberg, Heidelberg, Germany. His current research interests include 3-D biomedical image analysis, particularly landmark localization, vessel segmentation, cell segmentation, and image registration.

Hendrik von Tengg-Kobligk received the M.D. degree in medicine and Dr. Med. degree in radiology from University of Heidelberg, Heidelberg, Germany, in 2001 and 2003, respectively.

He is currently the Head of the Radiological Study Group "AORTA", University of Heidelberg and the German Cancer Research Center (DKFZ). He was a Senior Resident at DKFZ until 2009. From 2001 to 2003, he was a Researcher at National Institutes of Health, Clinical Center, Bethesda, MD, and joined The Ohio State University, Columbus, OH, as a Postdoctoral Researcher. His research interests include vascular cross-sectional imaging and image processing, particularly vessel segmentation, modeling, and image registration.

Verena Henninger received the M.D. degree in medicine from the University of Heidelberg, Heidelberg, Germany, in 2010, and has been working toward the Dr. Med. degree in radiology at the German Cancer Research Center (DKFZ) Heidelberg, Heidelberg, since 2006.

Her current research interests include the assessment of the thoracic aorta and age-related changes, improvement of stent-graft repair of thoracic aortic pathologies, MR angiography, and image postprocessing.

Fabian Rengier has been working toward the M.D. degree in medicine and the Dr. Med. degree in radiology from the University of Heidelberg, Heidelberg, Germany, since 2005.

He is currently a Research Fellow in the Department of Diagnostic and Interventional Radiology, University Hospital Heidelberg, Heidelberg, and also in the Department of Radiology, German Cancer Research Center Heidelberg. His research interests include new cardiovascular imaging and image postprocessing techniques.

Mr. Rengier was the recipient of scholarships from the German Research Foundation, The German National Academic Foundation, the German Academic Exchange Service, and the University of Heidelberg.

Hardy Schumacher received the Ph.D. degree from the Ludwig Maximilians University of Munich, Munich, Germany, in 1993, and the Habilitation degree from the University of Heidelberg, Heidelberg, Germany, in 2004.

He is currently a Professor of Surgery at the University of Heidelberg and the Director of the Clinic for Vascular and Endovascular Surgery and the Certified Vascular Center Rhein-Main, Academic Teaching General Hospital Hanau, University Frankfurt am Main, Germany. He has authored or coauthored more than 100 peer-reviewed scientific papers and more than 30 book chapters. His research interests include all aspects of aortic imaging and reconstruction with focus on endovascular repair.

Dittmar Böckler received the M.D. degree in medicine from the University of Erlangen, Germany, in 1993, and the Dr. Med. and Habilitation degrees in surgery from the University of Heidelberg, Heidelberg, Germany, in 1993 and 2005, respectively.

He is currently a Professor of Surgery and Head of the Department of Vascular and Endovascular Surgery, University of Heidelberg. His research interests include endovascular surgery of aortic pathologies.

Hans-Ulrich Kauczor received the M.D. degree in medicine from the University of Bonn, Bonn, Germany, in 1989, the Dr. Med. degree from the University of Köln, Köln, Germany, in 1991, and the Habilitation degree from the University Hospital Mainz, Mainz, Germany, in 1998.

In 1989, he joined the University Hospital Mainz for Radiology Residency. He is currently a Full Professor and Chairman of radiology at the University of Heidelberg, Heidelberg and the Medical Director in the Department of Diagnostic and Interventional Radiology. From 1996 to 2002, he was an Assistant Professor in the Department of Radiology, University of Mainz. In 2003, he became a Full Professor for Radiology and a Leader in the Department of Radiology, German Cancer Research Center (DKFZ), Heidelberg. Since 1990, he has authored or coauthored more than 350 publications. His current research interests include the field of computed tomography and MRI of the chest and oncology.

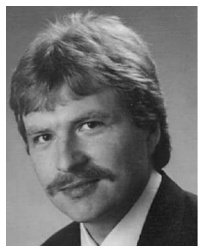

Karl Rohr received the degree in electrical engineering from the University of Karlsruhe (TH), Karlsruhe, Germany, and the Ph.D. and Habilitation degrees in computer science from the University of Hamburg, Hamburg, Germany, in 1994 and 1999, respectively.

He is currently an Associate Professor and Head of the Biomedical Computer Vision Group, University of Heidelberg and the German Cancer Research Center (DKFZ), Heidelberg, Germany. From 2000 to 2004, he was an Associate Professor at the International University in Germany, Bruchsal, Germany. In summer 1999, he was at the Surgical Planning Laboratory, Harvard Medical School, Boston, MA, as a Researcher. Since 2007, he has been a Guest Professor at the International University in Germany. His research interests include biomedical image analysis with focus on elastic registration, vessel segmentation, landmark localization, and tracking. He is the author of one book on *Landmark-Based Image Analysis* (Dordrecht, Netherlands: Kluwer Academic Publishers, 2001), which includes landmark localization and elastic registration. He has authored or coauthored more than 150 peer-reviewed scientific articles.

Dr. Rohr is an Associate Editor of IEEE TRANSACTIONS ON BIOMEDICAL ENGINEERING. He was engaged in the editorial board of the journal *Pattern Recognition*.